J. Mech. Phys. Solids 99 (2017) 471–482

Contents lists available at ScienceDirect

Journal of the Mechanics and Physics of Solids

journal homepage: www.elsevier.com/locate/jmps

Microscopic and macroscopic instabilities in hyperelastic fiber composites

Viacheslav Slesarenko[a,b], Stephan Rudykh[a,*]

[a] Department of Aerospace Engineering, Technion – Israel Institute of Technology, Haifa, Israel
[b] Lavrentyev Institute of Hydrodynamics of RAS, Novosibirsk, Russia

ARTICLE INFO

Keywords:
Finite deformation
Instability
Bifurcation
Fiber composites
Laminates
Microscopic instabilities
Loss of ellipticity

ABSTRACT

In this paper, we study the interplay between macroscopic and microscopic instabilities in 3D periodic fiber reinforced composites undergoing large deformations. We employ the Bloch-Floquet analysis to determine the onset of microscopic instabilities for composites with hyperelastic constituents. We show that the primary mode of buckling in the fiber composites is determined by the volume fraction of fibers and the contrast between elastic moduli of fiber and matrix phases. We find that for composites with volume fraction of fibers exceeding a threshold value, which depends on elastic modulus contrast, the primary buckling mode corresponds to the long wave or macroscopic instability. However, composites with a lower amount of fibers experience microscopic instabilities corresponding to wavy or helical buckling shapes. Buckling modes and critical wavelengths are shown to be highly tunable by material composition. A comparison between the instability behavior of 3D fiber composites and laminates, subjected to uniaxial compression, reveals the significant differences in critical strains, wavelengths, and transition points from macro- to microscopic instabilities in these composites.

1. Introduction

Composite materials have opened a new era in material science and engineering, allowing one to design materials with superior mechanical properties and unique functionalities. One of the most challenging problems in composite science is associated with the prediction of their failure. The phenomenon of local buckling or loss of stability has been historically considered as a failure mode, on par with delamination or fiber crashing (Christensen, 2005). In contrast with latter two modes, which are associated with loss of composite integrity, the buckling phenomenon can be exploited to create ordered internal structures. The ability to control the microstructure opens new ways to actively control the performance of materials (Ohzono and Monobe, 2012; Overvelde et al., 2012; Shan et al., 2015; Babaee et al., 2016). For example, Rudykh and Boyce (2014) showed, that the buckling of the interfacial layers can be utilized to create elastic wave bandgaps in layered materials. Recently, Slesarenko and Rudykh (2016) experimentally showed that the internal wavy patterns, appearing in layered composites with viscoelastic constituents undergoing compression, can be controlled by strain rate, thus, increasing the tunability of the composite microstructure.

The pioneering studies of Rosen (1967), Hill and Hutchinson (1975) laid the basis for the theoretical understanding of the elastic instability phenomenon in layered and fiber composites. In composite materials instabilities may develop at different length scales, thus, Triantafyllidis and Maker (1985) and, more recently, Nestorović and Triantafyllidis (2004) predicted the onsets of instabilities

* Corresponding author.
E-mail address: rudykh@technion.ac.il (S. Rudykh).

http://dx.doi.org/10.1016/j.jmps.2016.11.002
Received 7 July 2016; Received in revised form 27 October 2016; Accepted 1 November 2016
Available online 04 November 2016
0022-5096/ © 2016 Elsevier Ltd. All rights reserved.

in hyperelastic layered media at the microscopic and macroscopic length scales under plane-strain conditions. This phenomenon has been observed in experiments on the 3D printed layered materials (Li et al., 2013; Slesarenko and Rudykh, 2016). The onset of the macroscopic instabilities, characterized by wavelengths significantly larger than the microstructure characteristic size, can be predicted by the loss of ellipticity analysis requiring evaluation of the homogenized tensor of elastic moduli. Thus, for example, Qiu and Pence (1997), Merodio and Pence (2001), and Merodio and Ogden (2002) utilized this approach together with a phenomenological material model for transversely isotropic fiber composites in their analysis of the macroscopic stability. In a series of rigorous papers, Merodio and Ogden, (2003, 2005a, 2005b) showed that the loss of ellipticity is possible even under tensile loadings for incompressible and compressible material models satisfying certain conditions. An alternative way to estimate the onset of macroscopic instabilities is the usage of a micromechanics based homogenization (deBotton, 2005; Lopez-Pamies and Ponte-Castañeda, 2006a, 2006b; Agoras et al., 2009b). Agoras et al. (2009a), and Rudykh and deBotton (2012) employed the micromechanics based homogenization approaches, and they predicted the onset of macroscopic instabilities in hyperelastic fiber composites with incompressible (Agoras et al., 2009a; Rudykh and deBotton, 2012), and compressible (Rudykh and deBotton, 2012) isotropic hyperelastic phases. In particularly, an explicit expression for the onset of the macroscopic instabilities in hyperelastic fiber composites has been derived in terms of the properties of the constituents and volume fractions. For the composites with the considered isotropic hyperelastic phases, the loss of ellipticity is found to develop only under compressive loadings in the fiber direction.

Analysis of microscopic instabilities at smaller length scales, comparable with the characteristic dimensions of the microstructure, is a more challenging task that requires application of more involving techniques, such as Bloch-Floquet analysis. A rigorous study by Geymonat et al. (1993) showed the equivalence between the loss of ellipticity analysis (or macroscopic instability analysis) and the Bloch-Floquet analysis for the infinite wavelength. Nestorović and Triantafyllidis (2004) implemented the Bloch-Floquet technique into the finite element analysis and examined the macroscopic and microscopic stability in two-dimensional layered media, subjected to combinations of shear and compression deformations. The studies by Triantafyllidis et al. (2006), and Michel et al. (2010), considering 2D periodic composites under plane-strain deformations, showed the existence of macroscopic and microscopic instabilities in these composites. Once again, these studies are limited to 2D cases, and questions about the interplay between macroscopic and microscopic instabilities in 3D fiber composites, undergoing finite deformations in the fiber direction, remain open. At the same time, as it was shown for the 2D layered media (Triantafyllidis and Maker, 1985; Li et al., 2013; Slesarenko and Rudykh, 2016), microscopic instabilities may be the primary buckling mode in composites undergoing compression. In this study, we specifically focus on this important mode of compressive deformation along the fiber direction, and we analyze the onset of microscopic instabilities in 3D hyperelastic fiber composites and the associated buckling modes. Su et al. (2014) considered the behavior of a metallic rod embedded in an elastomeric matrix under compressive loading; in the framework of small strain linear elasticity wavy and coiled buckling modes were identified, and then realized for a Nitinol slender rod in an elastomeric matrix (Su et al., 2014). Here, we consider finitely deformed 3D fiber composites with hyperelastic phases, and, by making use of the Bloch-Floquet analysis superimposed on large deformations, we analyze the macroscopic and microscopic instabilities in these nonlinear composites. In particular, we find the conditions, under which microscopic instability may occur in the hyperelastic fiber composites subjected to compressive deformations along the fiber direction, and analyze the interplay between macroscopic and microscopic instabilities. We find that microscopic instabilities can develop earlier, and, depending on the material composition, these instabilities give rise to various buckling modes such as wavy patterns or even 3D helical structures. Finally, we compare the buckling behaviors of the 3D fiber composite and layered materials. Through the comparison, we show that these similar composites exhibit different instability characteristics, such as critical strains, wavelengths, and buckling modes, which are of importance for design of mechanotunable materials and structures.

2. Theoretical background

Consider a continuum body and identify each point in the undeformed configuration with its position vector $\mathbf{X}$. In the deformed body the new location of the corresponding points is defined by mapping function $\boldsymbol{x} = \boldsymbol{\chi}(\boldsymbol{X})$. The deformation gradient $\boldsymbol{F}$ is defined as $\boldsymbol{F} = \partial \boldsymbol{x}/\partial \boldsymbol{X}$ and its determinant as $J = det\boldsymbol{F}>0$. For a hyperelastic material, whose constitutive behavior can be described in terms of a strain energy-density function $W(\boldsymbol{F})$, the first Piola-Kirchoff stress tensor is given by

$$\boldsymbol{P} = \frac{\partial W(\boldsymbol{F})}{\partial \boldsymbol{F}}. \tag{1}$$

For an incompressible hyperelastic materials ($J = 1$) Eq. (1) modifies as

$$\boldsymbol{P} = \frac{\partial W(\boldsymbol{F})}{\partial \boldsymbol{F}} - p\boldsymbol{F}^{-T}, \tag{2}$$

where p is an unknown Lagrange multiplier.

The corresponding Cauchy ($\boldsymbol{\sigma}$) and the second Piola-Kirchhoff ($\boldsymbol{S}$) stress tensors are related to the first Piola-Kirchhoff tensor via $\boldsymbol{\sigma} = J^{-1}\boldsymbol{P}\boldsymbol{F}^T$ and $\boldsymbol{S} = \boldsymbol{F}^{-1}\boldsymbol{P}$, respectively. For homogeneous incompressible neo-Hookean materials, the strain energy function is given as

$$W = \frac{\mu}{2}(\boldsymbol{F} : \boldsymbol{F} - 3), \tag{3}$$

where μ is the initial shear modulus. The corresponding first Piola-Kirchhoff stress tensor is

$$\boldsymbol{P} = \mu\boldsymbol{F} - p\boldsymbol{F}^{-T}. \tag{4}$$

In the absence of body forces, the equation of motion can be written in the undeformed configuration as

$$Div\boldsymbol{P} = \rho_0 \frac{D^2\boldsymbol{\chi}}{Dt^2}, \tag{5}$$

where ρ_0 is the initial density of the material and the operator $D^2(\bullet)/Dt^2$ represents the material time derivative. When deformation is applied quasi-statically, Eq. (5) reads as

$$Div\boldsymbol{P} = 0. \tag{6}$$

Let us consider finitely deformed fiber composite with incompressible neo-Hookean constituents with shear moduli of fiber and matrix phases denoted by μ_f and μ_m, respectively, and with volume fraction of fibers denoted by v_f. The macroscopic average deformation gradient $\overline{\boldsymbol{F}}$ and the first Piola-Kirchhoff stress tensor can be expressed as

$$\overline{\boldsymbol{F}} = \frac{1}{V}\int_{\mathfrak{B}_0} \boldsymbol{F}(\boldsymbol{X})dV \qquad \overline{\boldsymbol{P}} = \frac{1}{V}\int_{\mathfrak{B}_0} \boldsymbol{P}(\boldsymbol{X})dV, \tag{7}$$

where $\mathfrak{B}_0$ represents the initial configuration of the body.

By utilizing an exact analytical solution, derived by deBotton et al. (2006), an effective homogenized strain energy function for transversely isotropic (TI) fiber composites can be written as

$$W^{eff}(\overline{\boldsymbol{F}}) = \frac{\overline{\mu}}{2}(\overline{\boldsymbol{F}} : \overline{\boldsymbol{F}} - 3) + \frac{\overline{\mu} - \widetilde{\mu}}{2}\left(I_4 + 2\sqrt{\frac{1}{I_4}} - 3\right), \tag{8}$$

where $I_4 = \boldsymbol{m}\overline{\boldsymbol{C}}\boldsymbol{m}$, $\overline{\boldsymbol{C}} = \overline{\boldsymbol{F}}^{\boldsymbol{T}}\overline{\boldsymbol{F}}$, and $\boldsymbol{m}$ denotes the initial fiber direction. The effective shear moduli of the TI composites are

$$\overline{\mu} = v_f\mu_f + (1 - v_f)\mu_m, \qquad \widetilde{\mu} = \frac{\mu_m((1+v_f)\mu_f + (1-v_f)\mu_m)}{(1-v_f)\mu_f + (1+v_f)\mu_m}. \tag{9}$$

Physically, the effective shear modulus $\widetilde{\mu}$ describes the response of the TI composites under shear deformations, while $\overline{\mu}$ describes the response under in-plane and out-of-plane tension (deBotton et al., 2006; deBotton and Hariton, 2006).

For a uniaxial deformation of incompressible neo-Hookean composites along the fibers direction $\boldsymbol{m}$ the corresponding deformation gradient is

$$\overline{\boldsymbol{F}} = \lambda^{-\frac{1}{2}}\boldsymbol{e}_1 \otimes \boldsymbol{e}_1 + \lambda^{-\frac{1}{2}}\boldsymbol{e}_2 \otimes \boldsymbol{e}_2 + \lambda\boldsymbol{e}_3 \otimes \boldsymbol{e}_3, \tag{10}$$

where λ is a stretch ratio in the fiber direction $\boldsymbol{m} = \boldsymbol{e}_3$. For the uniaxial loading, the non-zero component of the first Piola-Kirchhoff tensor is

$$\overline{P}_{33} = \overline{\mu}(\lambda - \lambda^{-2}). \tag{11}$$

To perform the macroscopic stability analysis, we consider incremental deformations superimposed on a finitely deformed state. The linearized constitutive law can be expressed as

$$\dot{\boldsymbol{P}} = \mathbb{A} : \dot{\boldsymbol{F}}, \tag{12}$$

where $\dot{\boldsymbol{F}}$ is an infinitesimal variation in the deformation gradient from the current configuration, and $\dot{\boldsymbol{P}}$ is the corresponding change in the first Piola-Kirchhoff stress tensor. The tensor of elastic moduli is

$$\mathbb{A} = \frac{\partial^2 W}{\partial\boldsymbol{F}\partial\boldsymbol{F}}. \tag{13}$$

If deformation is homogeneous, than $\mathbb{A}_{ijkl}$ is independent of $\boldsymbol{X}$, and the incremental equilibrium equation can be written in the form

$$\mathbb{A}_{ijkl}\frac{\partial^2 u_l}{\partial X_i \partial X_k} = 0, \tag{14}$$

where $\boldsymbol{u}$ is the incremental displacement associated with $\dot{\boldsymbol{F}}$. For incompressible materials the equilibrium equation takes form

$$\mathbb{A}_{ijkl}\frac{\partial^2 u_l}{\partial X_i \partial X_k} + \frac{\partial \dot{p}}{\partial x_j} = 0, \tag{15}$$

where $\dot{p}$ is an incremental change in p. The incompressibility condition implies

$$\nabla \cdot \boldsymbol{u} = 0. \tag{16}$$

2.1. Macroscopic instability

We seek a solution for (15) in the form

$$\boldsymbol{u} = \hat{\boldsymbol{u}} e^{ik\boldsymbol{x}\cdot\hat{\boldsymbol{n}}}, \quad \dot{p} = \hat{p}\, e^{ik\boldsymbol{x}\cdot\hat{\boldsymbol{n}}}, \tag{17}$$

where k is a wavenumber, $\hat{\boldsymbol{u}}$ and $\hat{\boldsymbol{n}}$ are two unit vectors.

The incompressibility constraint (16) leads to the requirement

$$\hat{\boldsymbol{n}}\cdot\hat{\boldsymbol{u}} = 0. \tag{18}$$

The incremental equilibrium (15) can be written in the form

$$\mathbb{A}^0_{ijkl}\frac{\partial^2 u_l}{\partial x_i \partial x_k} + \frac{\partial \dot{p}}{\partial x_j} = 0, \tag{19}$$

where

$$\mathbb{A}^0_{ijkl} = J^{-1}F_{i\alpha}F_{k\beta}\mathbb{A}_{\alpha j\beta l}. \tag{20}$$

Substitution of (17) into (19) results in

$$\boldsymbol{Q}\hat{\boldsymbol{u}} + i\hat{p}\,\hat{\boldsymbol{n}} = 0, \tag{21}$$

where $\boldsymbol{Q}$ is the acoustic tensor with components defined as

$$Q_{ij} = \mathbb{A}^0_{piqj}\hat{n}_p\hat{n}_q \tag{22}$$

The strong ellipticity condition implies that $Q_{ij}\hat{u}_i\hat{u}_j>0$ for all vectors $\hat{\boldsymbol{u}}$ and $\hat{\boldsymbol{n}}$ such that $\hat{\boldsymbol{n}}\otimes\hat{\boldsymbol{u}}\neq 0$. The macroscopic instability occurs at the first point along the loading path for any vectors $\hat{\boldsymbol{u}}$ and $\hat{\boldsymbol{n}}$, satisfying the equation $Q_{ij}\hat{u}_i\hat{u}_j=0$. Thus, for hyperelastic fiber composites, which behavior can be described by the effective energy function (10), the critical stretch ratio under compression deformation, corresponding to the onset of macroscopic instabilities can be expressed as

$$\lambda^{macr} = \left(1-\frac{\widetilde{\mu}}{\overline{\mu}}\right)^{\frac{1}{3}}. \tag{23}$$

2.2. Microscopic instability

As discussed by Triantafyllidis and Maker (1985) and Geymonat et al. (1993), instabilities may develop at different wavelengths ranging from the size of a typical heterogeneity to the size of the entire specimen. To analyze the *microscopic* instabilities, we employ the Bloch-Floquet technique, superimposed on finite deformations (Bertoldi et al., 2008; Geymonat et al., 1993; Triantafyllidis et al., 2006). We consider periodic unit cell with dimensions L, W, H, defined by the three orthogonal lattice vectors $\boldsymbol{g}_1$, $\boldsymbol{g}_2$, $\boldsymbol{g}_3$ (Fig. 1), that $|\boldsymbol{g}_1|=L$, $|\boldsymbol{g}_2|=W$, $|\boldsymbol{g}_3|=H$, where $|\bullet|$ denotes the length of the vector. The Bloch-Floquet condition relates the incremental displacement fields $\boldsymbol{u}$ via

$$\boldsymbol{u}(\boldsymbol{X}+\boldsymbol{R}) = \boldsymbol{u}(\boldsymbol{X})e^{i\boldsymbol{K}\cdot\boldsymbol{R}}, \tag{24}$$

where $\boldsymbol{K}= K_1\boldsymbol{g}_1+K_2\boldsymbol{g}_2+K_3\boldsymbol{g}_3$ is the Bloch wave vector, and $\boldsymbol{R} = R_1\boldsymbol{g}_1+R_2\boldsymbol{g}_2+R_3\boldsymbol{g}_3$ is an arbitrary vector with integer coordinates R_1, R_2, R_3. In general, the microscopic instabilities may lead to a loss of the original periodicity, resulting in new periodicity with different lengths in all three dimensions (Babaee et al., 2013). However, here we limit our consideration only to the case, when the composite maintains the existed periodicity in ($\boldsymbol{g}_1$, $\boldsymbol{g}_2$) plane. This case corresponds to the Bloch wave vector $\boldsymbol{K} = (2\pi, 2\pi, K_3)$. The numerical Bloch-Floquet analysis (Bertoldi et al., 2008) has been implemented in a finite element based code as described next.

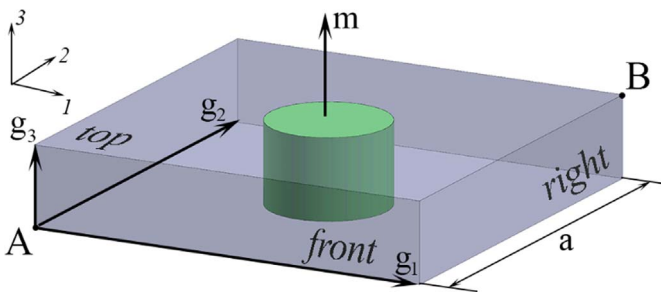


Fig. 1. Unit cell of periodical fiber composite.

3. Numerical simulations

Numerical simulations are conducted with the help of FE code COMSOL 4.2a. A representative volume element (RVE), used in calculations, is shown in Fig. 1. We consider the RVE with the dimensions $L = W = a$, $H = 0.1a$. Note that the height of the unit cell H is chosen to be ten times smaller than its width and length. This choice of the RVE geometry is motivated by computational efficiency, and by the need for eliminating redundant eigenvalues, which may appear as the result of boundary conditions, imposed on the top and bottom faces of the unit cell (Aberg and Gudmundson, 1997; García and Fernández-Álvarez, 2015). The materials of fiber and matrix are defined by neo-Hookean strain-energy function, integrated in COMSOL as

$$W = \frac{1}{2}\mu(I_1(\boldsymbol{C})-3)-\mu \ln J+\frac{1}{2}\Lambda(\ln J)^2, \tag{25}$$

where Λ is the first Lame constant. To maintain the nearly incompressible behavior of the constituents, we set a high ratio between the shear modulus and the first Lame constant, in particular $\Lambda=1000\mu$ is used in our simulations. We performed a mesh sensitivity analysis and determined that the unit cell, containing 10^4 elements, provides the values of critical stretch ratio with the error less than $5\cdot10^{-4}$.

The procedure for identifying the onset of microscopic instabilities and associated wavenumbers is performed in two steps. First, the unit cell undergoes static finite deformations, defined by the imposed periodic boundary conditions. Second, the eigenvalue problem is solved for the deformed unit cell with superimposed Bloch-Floquet boundary conditions. More specifically, the following periodic boundary conditions are imposed on the node displacement on the faces of the unit cell at each step:

Step 1.

$$\begin{cases} u_1|_{right}=u_1|_{left}+u_1|_B \\ u_2|_{right}=u_2|_{left} \\ u_3|_{right}=u_3|_{left} \end{cases} \quad \begin{cases} u_1|_{back}=u_1|_{front} \\ u_2|_{back}=u_2|_{front}+u_2|_B \\ u_3|_{back}=u_3|_{front} \end{cases} \quad \begin{cases} u_1|_{top}=u_1|_{bottom} \\ u_2|_{top}=u_2|_{bottom} \\ u_3|_{top}=u_3|_{bottom}-\varepsilon\cdot H \\ u_1|_A=u_2|_A=u_3|_A=0 \end{cases} \tag{26}$$

Here, the indexes *left, right, top and bottom* denote the faces of the unit cell; A and B correspond to the nodes at the corners of unit cell (see Fig. 1). Note that the compressive strain $\varepsilon = |1-\lambda|$ is defined as a positive value. The resulting stiffness matrix, corresponding to the applied strain ε, is stored for further solution of the eigenvalue problem at step 2.

Step 2.

$$\begin{cases} u_1|_{back}=u_1|_{front} \\ u_2|_{back}=u_2|_{front} \\ u_3|_{back}=u_3|_{front} \end{cases} \quad \begin{cases} u_1|_{right}=u_1|_{left} \\ u_2|_{right}=u_2|_{left} \\ u_3|_{right}=u_3|_{left} \end{cases} \quad \begin{cases} u_1|_{top}=u_1|_{bottom}e^{ik_3H\cdot 2\pi} \\ u_2|_{top}=u_2|_{bottom}e^{ik_3H\cdot 2\pi} \\ u_3|_{top}=u_3|_{bottom}e^{ik_3H\cdot 2\pi} \end{cases} \tag{27}$$

Here, $k_3 = K_3/2\pi$ corresponds to the third component of the Bloch wave vector $\boldsymbol{K}$.

The eigenvalue problem is solved for a range of k_3 values, more specifically, we scan the k_3 values from 0 to 5 with a step of 0.025, until the lowest eigenvalue becomes zero. The wavenumber k_3, corresponding to this appearance of a zero eigenvalue, is denoted by k_3^{cr}. If for the considered range of k_3 values, only positive eigenvalues appear, than the applied strain is increased, and steps 1 and 2 are repeated until the critical strain and critical wavenumber are identified.

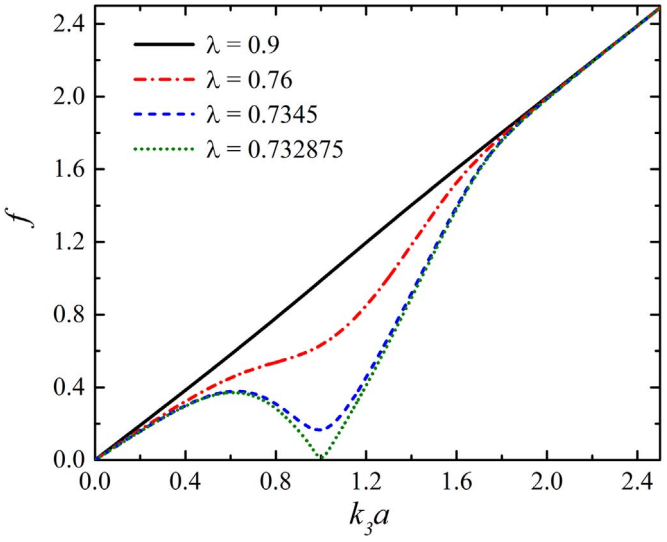


Fig. 2. Dispersion curves for the 3D fiber composite with $v_f = 0.02$ and $\kappa = 15$. The composite is subjected to different levels of deformation.

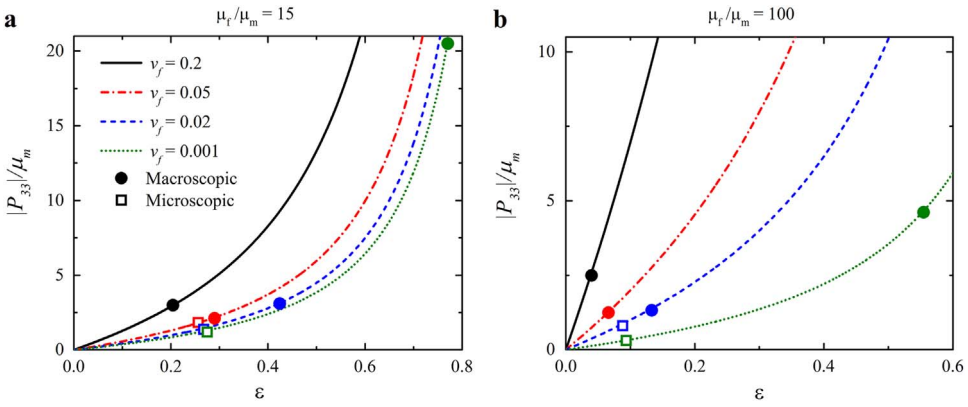


Fig. 3. Stress-strain curves for the fiber composites with $\kappa = 15$ (a) and $\kappa = 100$ (b). Circle and square symbols indicate the onsets of macroscopic and microscopic instabilities, respectively.

Fig. 2 illustrates the described numerical procedure, showing a typical evolution of the dispersion curves with applied deformation. Fig. 2 presents the dependence of the lowest normalized eigenfrequency $f = \frac{\omega}{2\pi}\sqrt{\rho/\tilde{\mu}}$ on the wavenumber k_3 for the fiber composite with volume fraction of fibers $v_f = 0.02$ and shear modulus contrast $\kappa = \mu_f/\mu_m$=15, with the identical densities of the matrix and fiber phases $\rho = \rho_m = \rho_f$. We observe that the black continuous curve, corresponding to the deformed state of $\lambda = 0.9$ ($\varepsilon = 0.1$), intersects x-axis only at the point (0,0), which corresponds to a trivial rigid body motion. While the black continuous curve in Fig. 2 is linear, a subsequent increase in compressive loading leads to a pronounced dispersion – non-linear dependence of the eigenfrequency on the wavenumber – visible for stretch ratios $\lambda = 0.76$ (red dash-dotted curve) and $\lambda = 0.7345$ (blue dashed curve). Eventually, when a critical stretch ratio λ^{cr} is achieved, a zero eigenvalue appears at a specific wavenumber $k_3^{cr} \neq 0$ (see the green dotted curve in Fig. 2). This compressive strain level corresponds to the onset of microscopic instabilities, and the value of k_3^{cr} defines the geometry of the buckling mode. The macroscopic instability corresponds to the long wave limit or $k_3^{cr} \to 0$. In the numerical simulations this limit is approximately captured by assigning small enough values of k_3.

4. Macroscopic and microscopic instabilities in 3D fiber composites

We start from considering the macroscopic response of the fiber composites, subjected to uniaxial compressive loading (10). The stress-strain curves, calculated with the help of expression (11) for the composites with the shear modulus contrast of $\kappa = 15$ and $\kappa = 100$, are shown in Fig. 3a and b, respectively.

We observe the expected stiffening of the composites with an increase in the volume fraction of fibers (compare the black continuous curve for $v_f = 0.2$ with the blue dashed curve for $v_f = 0.02$). We note that reported stress-strain results are in excellent agreement with the numerical simulation results for the achievable in FE simulations strains (at least until the onset of instability). The square and circle symbols denote the critical strains, corresponding to the onsets of microscopic and macroscopic instabilities, respectively. We observe that the difference between the critical strains, corresponding to the onsets of microscopic and macroscopic instabilities, decreases with an increase in amount of fibers, and for a large enough volume fractions of the fibers, the primary instability develops at a long wave mode. For instance, for the composite with shear modulus contrast $\kappa = 15$ and volume fraction of fibers $v_f = 0.001$ (green dotted curve in Fig. 3a), the onset of macroscopic instability corresponds to the compression strain $\varepsilon^{(macro)} = 0.77$, while microscopic buckling occurs much earlier at the critical strain $\varepsilon^{(micro)} = 0.275$. Thus, the gap between the onsets of microscopic and macroscopic instabilities is about 0.5. An increase in volume fraction of fibers up to $v_f = 0.05$ leads to a decrease of this gap down to 0.033 (critical strains for macroscopic and microscopic instabilities are equal to $\varepsilon^{(macro)} = 0.29$ and $\varepsilon^{(micro)} = 0.257$, respectively). Finally, for the composite with $v_f = 0.2$, the macroscopic instability occurs prior to microscopic one at the strain level $\varepsilon^{(macro)} = 0.205$. Thus, for fiber composites with small volume fractions of fibers, the primary instability mode corresponds to short wavelengths, while composites with large amount of fibers experience macroscopic instability when the critical strain is achieved.

To highlight the influence of the constituents volume fractions on the onsets of microscopic and macroscopic instabilities, in Fig. 4 we plot the critical stretch as a function of the fiber volume fraction. The critical stretches are calculates for the composites with $\kappa = 100$ (black continuous curve) and $\kappa = 15$ (red continuous curve).

The continuous curves correspond to the onsets of macroscopic instabilities, while dotted curves represent the onsets of microscopic instabilities. As expected, the composites with high contrasts in shear moduli, experience instabilities at lower compressive loadings (compare the black and the red continuous curves in Fig. 4). While the macroscopic curves show a significant decrease of the critical stretch ratio at the region of small volume fractions of the fibers, the microscopic curves branches out from the macroscopic curves. A decrease in the microscopic critical stretch with a decrease in fibers volume fraction is significantly slower than the one observed for the critical macroscopic stretch ratio at this region of v_f. For composites with the volume fractions, which does not exceed specific threshold value (v^{th}), the primary mode of buckling corresponds to microscopic instability. At the same time, for composites with the fiber volume fraction $v_f > v^{th}$, the primary instability mode is associated with the long wave mode,

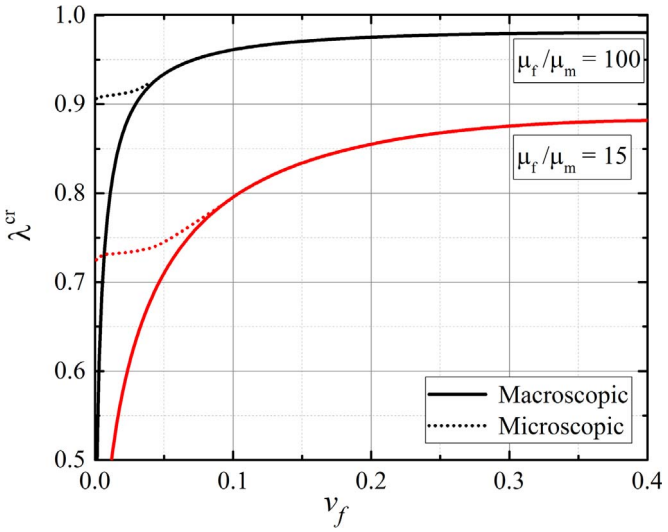


Fig. 4. Dependence of the macroscopic (continuous curves) and microscopic (dotted curves) critical stretch ratios on the volume fraction of stiffer phase (v_f) for the composites with shear modulus contrasts κ=15 (red curves) and κ =100 (black curves). (For interpretation of the references to color in this figure legend, the reader is referred to the web version of this article.)

corresponding to $k_3^{cr}\to 0$. The interplay between the microscopic and macroscopic instabilities, observed in the 3D fiber composites, is similar to the behavior of periodic laminates, observed experimentally by Li et al. (2013) and predicted theoretically by Triantafyllidis and Maker (1985). However, the important characteristics of the microscopic instabilities such as critical stretch ratio and critical wavelengths are significantly different in these composites as we illustrate in the next section.

Next, we study the influence of the contrast in shear moduli between fiber and matrix phases, on the stability of the fiber composites. In Fig. 5, we plot the critical stretch as a function of the shear modulus contrast κ. The black squares, red triangles and blue circles represent the critical stretches for the composites with volume fractions of fibers v_f = 0.02, 0.06, and 0.4, respectively. In Fig. 5 the half-filled symbols denote the approximate stiffness ratio at which the primary buckling mode switches from the macroscopic to a microscopic one. We observe that the critical stretch ratio (λ^{cr}) decreases with a decrease in the shear modulus contrast. Consistently with the previous observations, we find out that the composite with large volume fraction of fibers, experiences macroscopic instability, see, for example, the blue circles, corresponding to the composite with v_f = 0.4 (note that the simulations are performed for the range of contrast in shear moduli exceeding 10). However, composites with small volume fractions exhibit a switch from the long wave mode to a finite wavelength mode, when the shear modulus contrast is decreased beyond a threshold value, see for example the black squares and red triangles, corresponding to v_f = 0.02 or 0.06, respectively.

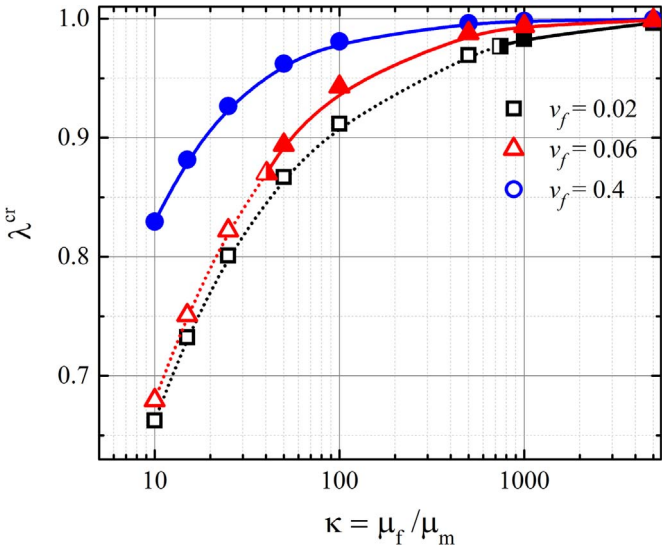


Fig. 5. Dependence of critical stretch ratio λ^{cr} on the shear modulus contrast κ. Continuous curves and solid symbols correspond to the onsets of macroscopic instabilities, while dotted curves and hollow symbols correspond to the onsets of microscopic instabilities. Half-filled symbols represent the approximate value of κ, associated with the transition in the instability modes.

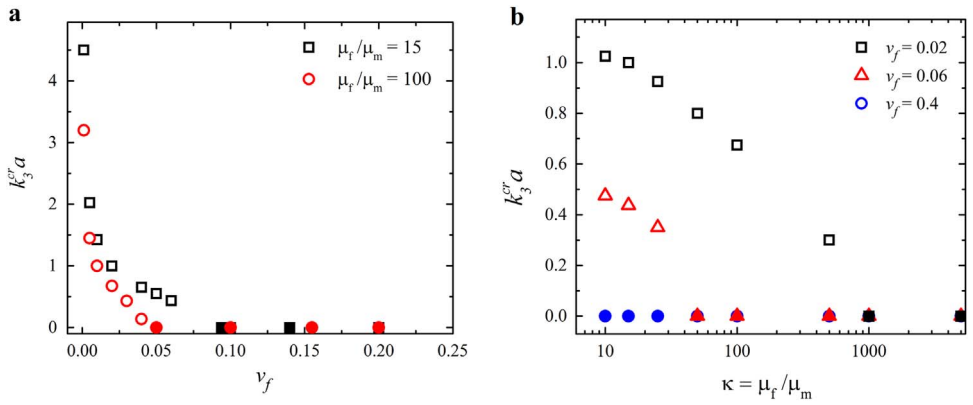


Fig. 6. Dependence of critical wavenumber (k_3^{cr}) on the fibers volume fraction v_f (a) and the shear modulus contrast κ (b).

To analyze the dependence of the critical wavelength on the material composition, we plot the critical wavenumber as a function of the fibers volume fraction v_f, and contrast in shear moduli κ. In Fig. 6a, the results are presented for composites with the contrast in shear moduli $\kappa = 15$ (squares), and $\kappa = 100$ (circles). For the fiber composites with large and moderate volume fractions of fibers, we observe that the critical wavenumber $k_3^{cr} \to 0$ corresponds to the long wave mode of instability. However, after some threshold value of v_f, the critical wavenumber k_3^{cr} starts increasing with a further decrease in fibers volume fraction. This transition corresponds to the switch at which the microscopic instability starts developing earlier than the long wave instability. However, at this transition region the critical stretches, corresponding to the onsets of the macroscopic and microscopic instabilities, take very close values, making it difficult to determine numerically; arguable, from an experimental point of view, it means that for composite with fiber volume fraction value close enough to the threshold value v^{th}, the instability wavelength would be defined by some imperfection, appeared during fabrication or testing. Nevertheless, Fig. 6a allows us to conclude that the threshold value v^{th}, separating the onsets of macroscopic and microscopic instabilities, increases with a decrease in the shear modulus contrast. We note that the increase in the wavenumber becomes even more significant with a decrease of fiber volume fraction towards the dilute limit.

Fig. 6b shows the critical wavenumber as a function of the shear modulus contrast for composites with fiber volume fraction $v_f = 0.02$ (squares), 0.06 (triangles), and 0.4 (circles). For the composites with large volume fractions, exceeding the threshold values for the considered shear modulus contrast ratio, the instability develops only at the long wave mode. This situation corresponds to the results for the composite with $v_f = 0.4$ (see the blue circles in Fig. 6b). However, for composites with smaller fiber volume fractions, less than a threshold value ($v_f < v_{th}$), we observe an increase in the wavenumber with a decrease in the shear modulus contrast. We note that the composites with smaller volume fractions are characterized by larger critical wavenumbers, and therefore by lower critical wavelengths (compare the red triangles and the black circles in Fig. 6b). In particular, the composites with volume fraction of the fibers $v_f = 0.06$ attain the critical wavenumber $k_3^{cr}a \approx 0.44$, while the composite with $v_f = 0.02$ experience the microscopic instabilities with the critical wavenumber $k_3^{cr}a \approx 1.03$ for shear modulus ratio $\kappa = 10$. Thus, the instability patterns can

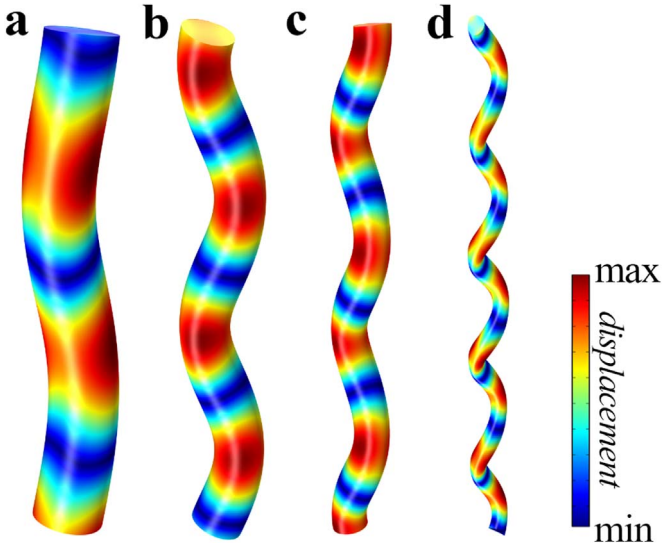


Fig. 7. Buckling modes of fibers in composites with κ=15 and $v_f = 0.02$ (a), 0.01 (b), 0.005 (c) and 0.001 (d). The colors represent the relative in-plane displacement of the points on the surface of buckled fiber from their position in the undeformed fiber.

be significantly tuned by the material composition.

Fig. 7 presents the different buckling patterns, which may occur as results of microscopic instabilities in the composites with various v_f. To illustrate the appearance of such patterns we use a larger unit cell with an increased height $H = 1.2a$, containing about $8{\cdot}10^4$ elements. Indeed, the critical stretch ratios, obtained for the increased unit cell, are identical to the values obtained for the unit cell with the height of $0.1a$. The patterns are shown for composites with shear modulus contrast $\kappa = 15$, and with various volume fractions of fibers $v_f = 0.02$ (a), 0.01 (b), 0.005 (c), and 0.001 (d). The colors represent the relative in-plane displacement of the points on the surface of buckled fiber from their position in the undeformed fiber. In accordance to the reported increase in k_3^{cr} with a decrease in fibers volume fraction, we observe the evolution of the buckling patterns as the volume fraction decreases from 0.02 to 0.001.

For composite with $v_f = 0.001$ we have 3–4 full waves, fitted in the unit cell, while for composite with $v_f = 0.02$, only one wave appears. Remarkably, for the composites with a small amount of fibers the corresponding microscopic buckling pattern develops simultaneously in two directions, giving rise to the formation of a helical structure (see Fig. 7d). For composites with larger v_f, we do not observe this phenomenon; and the primary microscopic instability modes appear in one plane for the composites with larger volume fractions of the fibers.

5. Comparison of the instabilities in 3D fiber composites and laminates

In this section, we provide a comparison between our new results for microscopic instabilities in finitely deformed 3D fiber composites versus the results for 2D laminates obtained for the plane-strain deformation. In addition, we provide the results for the periodic laminates subjected to the corresponding 3D deformation, and compare these results in terms of critical stretches and critical wavelengths. In particular, we consider the layered and fiber composites, consisting of the two neo-Hookean phases with shear moduli μ_f for stiff fibers or layers, and μ_m for soft matrix, respectively. The volume fraction of fibers/layers is denoted by v_f.

5.1. Macroscopic instabilities

To calculate the onset of macroscopic instabilities in 3D fiber composite with incompressible neo-Hookean constituents we use the explicit expression (13). The onset of macroscopic instabilities in layered composites under three-dimensional deformations developing due to a uniaxial compression in the direction of layers can be estimated based on an exact solution for finitely deformed laminates (deBotton, 2005; Galich et al., 2016)

$$\lambda^{macr} = \left(1-\frac{\widehat{\mu}}{\overline{\mu}}\right)^{\frac{1}{3}}, \tag{28}$$

where $\overline{\mu}$ and $\widehat{\mu}$ are effective shear modules. For the case of plane-strain compression along layers direction the critical stretch ratio in 2D layered composites can be calculated (Triantafyllidis and Maker, 1985) as

$$\lambda^{macr} = \left(1-\frac{\widehat{\mu}}{\overline{\mu}}\right)^{\frac{1}{4}} \tag{29}$$

Note that the effective moduli $\overline{\mu}$ and $\widehat{\mu}$ for layered composites have the same physical meanings as the effective moduli $\overline{\mu}$ and $\widetilde{\mu}$ for fiber composites (9), respectively. However, for layered composites, the expression for the effective shear modulus $\widehat{\mu}$ is different, and it takes the form

$$\widehat{\mu} = \left(\frac{\mu_f}{v_f} + \frac{\mu_m}{v_m}\right)^{-1} \tag{30}$$

Thus, despite the similar form of the Eqs. (28) and (13), the macroscopic instabilities for fiber and layered composites occur at different stretch ratios. This difference is illustrated in Fig. 8.

Fig. 8 shows the dependencies of the critical stretch ratios on the fibers/layers volume fraction for the fibers/layers composites with the shear modulus contrast $\kappa = 15$. We observe that the macroscopic instabilities develop earlier (at larger critical stretch ratios) in the layered composites subjected to plane-strain deformation; while the 3D fiber composites require larger compressive deformation to achieve the onset of macroscopic instability. Fig. 8 highlights a distinct feature of the 3D fiber composites, which exhibit different macroscopic stability properties for large and dilute concentrations of the fibers; whereas the stability curves obtained for the finitely deformed laminates are symmetric with respect to $v_f = 0.5$. For example, in layered composites with $v_f = 0.3$ and $v_f = 0.7$ the critical stretch ratios have the same value, whereas the critical stretch ratios in corresponding 3D fiber composites are not equal. Thus, the soft and stiff phases in 3D fiber composites are not interchangeable in terms of instability analysis even under homogenization approach. While for layered and fiber composites with incompressible neo-Hookean constituents explicit expressions for the onsets of macroscopic instabilities under uniaxial compression can be derived, the analysis of microscopic instabilities requires a more complex analysis.

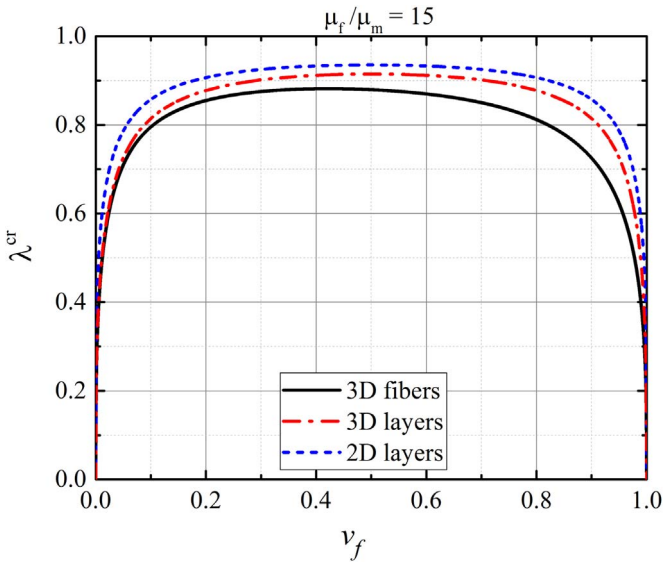


Fig. 8. Dependencies of macroscopic critical stretch ratios on the fibers/layers volume fraction for the fiber (solid black curve) and layered composites (dash-dotted red curve), subjected to uniaxial compression, and layered composites, subjected to compression along the layers direction in plane-strain conditions (blue dashed curve). (For interpretation of the references to color in this figure legend, the reader is referred to the web version of this article.)

5.2. Microscopic instabilities

To identify the onset of microscopic instability, and the corresponding critical wavelengths, the Bloch-Floquet FEA technique (described in Sec. Numerical Simulations) has been applied for the analysis of layered composites subjected to (i) uniaxial compression, and (ii) plane-strain compression. Fig. 9 shows the dependencies of the critical stretch ratios for the onset of microscopic and macroscopic instabilities on the fibers/layers volume fraction v_f for composites with shear modulus contrast $\kappa = 15$ (a) and $\kappa = 100$ (b). The continuous, dashed-dotted, and dashed curves correspond to the onset of macroscopic instability, while the dotted curves are for the microscopic instabilities.

We observe that the layered composites under plane-strain uniaxial compression require lower compressive strains to develop instabilities, as compared to the laminates that are allowed to deform in 3D. The microscopic instabilities in 3D fiber composites develop significantly later (at lower critical stretches). At the same time, despite close values of the critical stretches of macroscopic instabilities in layered and fiber composites, subjected to a uniaxial compression, the difference between the onsets of microscopic instabilities is rather significant. For example, in fiber composite with $\kappa = 100$ and $v_f = 0.025$, microscopic instability occurs at the strain level of $\varepsilon \approx 8.6\%$, while the corresponding laminate exhibits microscopic instability much earlier at $\varepsilon \approx 4.3\%$ (two times smaller strain); whereas the upper bonds for critical stretch ratios, estimated by the onsets of macroscopic instabilities, are almost identical for these two geometries ($\varepsilon \approx 11\%$). Moreover, the threshold value of volume fraction v^{th}, at which the primary mode of instability switches from macroscopic to microscopic, differs significantly in the composites. One may see in Fig. 9, that v^{th} is much lower for the fiber composites, than for the layered composites. For example, for composite with $\kappa = 100$ the threshold value $v^{th} \approx 0.04$ in fiber composite (black solid curve) and $v^{th} \approx 0.09$ in layered composite (red dash-dotted curve).

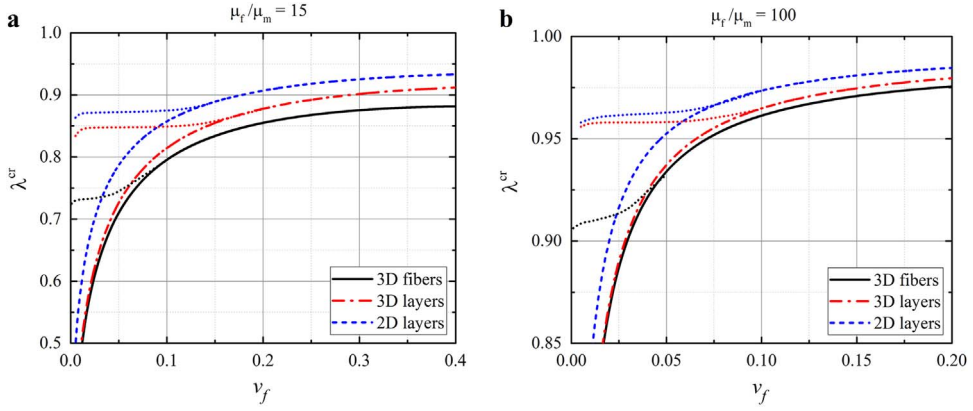


Fig. 9. Dependencies of the macroscopic and microscopic (dotted curves) critical stretch ratios on the volume fraction of rigid phase (v_f) for the fiber and layered composites with shear modulus contrasts κ=15 (a) and κ =100 (b).

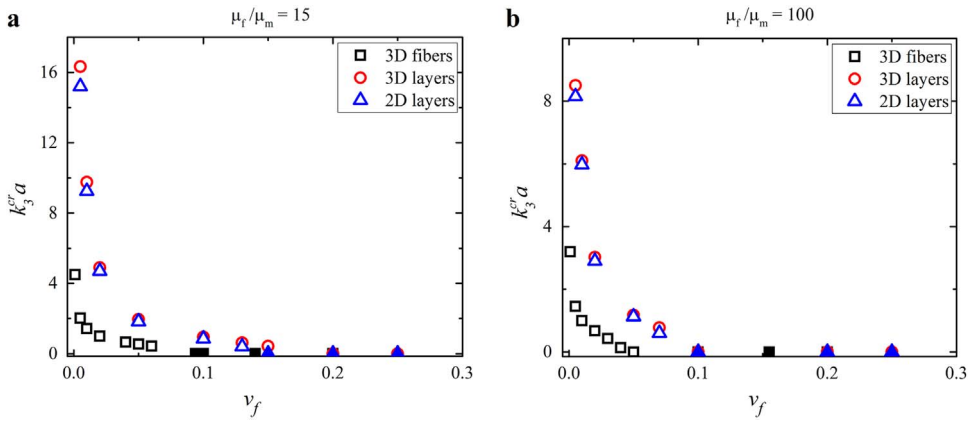


Fig. 10. Dependencies of the critical wavenumber (k_3^{cr}) on the on the volume fraction of rigid phase (v_f) for the fiber and layered composites with shear modulus contrasts κ=15 (a) and κ =100 (b), subjected to different deformation modes.

Furthermore, the wavenumbers and wavelengths of the corresponding buckling patterns significantly depend on the composite's geometry. Fig. 10 illustrates the dependencies of wavenumbers on the volume fraction for 3D fiber composites (black squares), laminates in plane-strain (blue triangles), and layered composites under 3D uniaxial compression (red circles). The results are shown for composites with the contrast in shear moduli κ = 15 (Fig. 10a) and κ = 100 (Fig. 10b). We find that the values of the corresponding wavenumbers for layered composites, subjected to uniaxial compression (red circles) and compression in plane-strain conditions (blue triangles), are very close. However, for 3D fiber composites with volume fractions identical to the layered composites, the corresponding wavenumber is several times lower than the wavenumber for layered composite. For instance, the wavenumber corresponding to the microscopic instability in the layered composite with $\kappa = 100$ and $v_f = 0.01$, is six times larger than the wavenumber in the fiber composite with the same amount of the stiffer phase and the same value of shear modulus contrast ($k_3^{cr}a \approx 6.1$ for laminates versus $k_3^{cr}a \approx 1.0$ for 3D fiber composites). Thus, these similar composites with identical amounts of phase materials develop very different patterns in buckling. At the same time, as opposite to layered composites, the fiber reinforced composites potentially are able to buckle in two dimensions with formation of non-planar patterns, which can be beneficial for particular applications, such as design of tunable acoustic metamaterials.

6. Conclusions

We examined the microscopic and macroscopic stability of the 3D fiber composites with hyperelastic phases, subjected to finite strains. By application of the Bloch-Floquet analysis, superimposed on finite deformations, we identified the critical stretches, corresponding to the onsets of instabilities. Our results showed that the critical stretch depends on the volume fraction of fibers and the contrast in shear moduli of the constituents. While for the long wave limit, the critical stretch was found to rapidly decrease with a decrease of the amount of fibers, the microscopic instability analysis showed that the instability at finite wavelengths develop significantly earlier for composites with small volume fractions of fibers. We found the existence of the threshold value of the fibers volume fraction v^{th}, at which the primary buckling mode switches from macroscopic instability to the microscopic one. Thus, for composites with volume fractions exceeding the threshold value, $v_f > v^{th}$, the long wave mode instability develops first, while for composites with fiber volume fraction smaller that a threshold value, $v_f < v^{th}$, the primary instability mode is associated with microscopic instability. The threshold value v^{th} was found to decrease with an increase in the shear modulus contrast. The critical wavenumber and wavelength strongly depend on the material composition. First, we observed a switch from the long wave mode, $k_3^{cr} \to 0$, to finite wavelength instabilities at a threshold point. Second, beyond the threshold the critical wavenumber was found to increase with a decrease in the fiber volume fraction and in the contrast in phase shear moduli.

Finally, we compared our results for microscopic instabilities in 3D fiber composites with the layered composites, and we found several important differences. In particular, the layered materials are found to be prone to the microscopic instability as compared to 3D fiber composites that develop instabilities at lower critical stretch ratios. Next, the threshold fibers/layers volume fraction v^{th}, for which a transition between macroscopic and microscopic instabilities occurs, is significantly lower in fiber composites. This leads to the noticeable difference in the wavelength of forming wavy patterns in fiber and layered composites.

The finite wavelength instabilities could result in appearance of wavy patterns or even 3D helical structures in composites with small volume fraction of the fibers. These instability induced-tunable microstructure transformations can be exploited for designing tunable materials with switchable functionalities.

Acknowledgements

This work was supported by the Israel Science Foundation (grants No1550/15 and 1973/15). Stephan Rudykh gratefully acknowledges the support of Taub Foundation through the Horev Fellowship – Leaders in Science and Technology. Viacheslav

Slesarenko thanks the Russian Science Foundation for support (through project 15-11-10000) of FE computations.

References

Aberg, M., Gudmundson, P., 1997. The usage of standard finite element codes for computation of dispersion relations in materials with periodic microstructure. J. Acoust. Soc. Am. 102, 2007–2013.

Agoras, M., Lopez-Pamies, O., Ponte Castañeda, P., 2009a. Onset of macroscopic instabilities in fiber-reinforced elastomers at finite strain. J. Mech. Phys. Solids 57, 1828–1850.

Agoras, M., Lopez-Pamies, O., Ponte Castañeda, P., 2009b. A general hyperelastic model for incompressible fiber-reinforced elastomers. J. Mech. Phys. Solids 57, 268–286.

Babaee, S., Shim, J., Weaver, J.C., Chen, E.R., Patel, N., Bertoldi, K., 2013. 3D soft metamaterials with negative poisson's ratio. Adv. Mater. 25, 5044–5049.

Babaee, S., Viard, N., Wang, P., Fang, N.X., Bertoldi, K., 2016. Harnessing Deformation to Switch on and off the Propagation of Sound. Adv. Mater. 28, 1631–1635.

Bertoldi, K., Boyce, M.C., Deschanel, S., Prange, S.M., Mullin, T., 2008. Mechanics of deformation-triggered pattern transformations and superelastic behavior in periodic elastomeric structures. J. Mech. Phys. Solids 56, 2642–2668.

Christensen, R.M., 2005. Mechanics of Composite Materials. Dover Publications, Mineola, N.Y., USA.

deBotton, G., 2005. Transversely isotropic sequentially laminated composites in finite elasticity. J. Mech. Phys. Solids 53, 1334–1361.

deBotton, G., Hariton, I., 2006. Out-of-plane shear deformation of a neo-Hookean fiber composite. Phys. Lett. Sect. A Gen. At. Solid State Phys. 354, 156–160.

deBotton, G., Hariton, I., Socolsky, E.A., 2006. Neo-Hookean fiber-reinforced composites in finite elasticity. J. Mech. Phys. Solids 54, 533–559.

Galich, P., Fang, N.X., Boyce, M.C., Rudykh, S., 2017. Elastic wave propagation in finitely deformed layered materials. J. Mech. Phys. Solids 98, 390–410.

García, P.G., Fernández-Álvarez, J.-P., 2015. Floquet-Bloch Theory and Its Application to the Dispersion Curves of Nonperiodic Layered Systems. Math. Probl. Eng. 2015, 12.

Geymonat, G., Müller, S., Triantafyllidis, N., 1993. Homogenization of nonlinearly elastic materials, microscopic bifurcation and macroscopic loss of rank-one convexity. Arch. Ration. Mech. Anal. 122, 231–290.

Hill, R., Hutchinson, J.W., 1975. Bifurcation phenomena in the plane tension test. J. Mech. Phys. Solids 23, 239–264.

Li, Y., Kaynia, N., Rudykh, S., Boyce, M.C., 2013. Wrinkling of Interfacial Layers in Stratified Composites. Adv. Eng. Mater. 15, 921–926.

Lopez-Pamies, O., Castañeda, P.P., 2006a. On the overall behavior, microstructure evolution, and macroscopic stability in reinforced rubbers at large deformations: i — Theory. J. Mech. Phys. Solids 54, 807–830.

Lopez-Pamies, O., Castañeda, P.P., 2006b. On the overall behavior, microstructure evolution, and macroscopic stability in reinforced rubbers at large deformations: ii - Application to cylindrical fibers. J. Mech. Phys. Solids 54, 831–863.

Merodio, J., Ogden, R.W., 2005a. Tensile instabilities and ellipticity in fiber-reinforced compressible non-linearly elastic solids. Int. J. Eng. Sci. 43, 697–706.

Merodio, J., Ogden, R.W., 2005b. Remarks on instabilities and ellipticity for a fiber-reinforced compressible nonlinearly elastic solid under plane deformation. Quaterly Appl. Math. LXIII, 325–333.

Merodio, J., Ogden, R.W., 2003. Instabilities and loss of ellipticity in fiber-reinforced compressible non-linearly elastic solids under plane deformation. Int. J. Solids Struct. 40, 4707–4727.

Merodio, J., Ogden, R.W., 2002. Material instabilities in fiber-reinforced nonlinearly elastic solids under plane deformation. Arch. Mech. 54, 525–552.

Merodio, J., Pence, T.J., 2001. Kink surfaces in a directionally reinforced neo-Hookean material under plane deformation: ii. Kink band stability and maximally dissipative band broadening. J. Elast. 62, 145–170.

Michel, J.C., Lopez-Pamies, O., Ponte Castañeda, P., Triantafyllidis, N., 2010. Microscopic and macroscopic instabilities in finitely strained fiber-reinforced elastomers. J. Mech. Phys. Solids 58, 1776–1803.

Nestorović, M.D.D., Triantafyllidis, N., 2004. Onset of failure in finitely strained layered composites subjected to combined normal and shear loading. J. Mech. Phys. Solids 52, 941–974.

Ohzono, T., Monobe, H., 2012. Microwrinkles: shape-tunability and applications. J. Colloid Interface Sci. 368, 1–8.

Overvelde, J.T.B., Shan, S., Bertoldi, K., 2012. Compaction Through Buckling in 2D Periodic, Soft and Porous Structures: Effect of Pore Shape. Adv. Mater. 24, 2337–2342.

Qiu, G.Y., Pence, T.J., 1997. Loss of Ellipticity in Plane Deformations of a Simple Directionally Reinforced Incompressible Nonlinearly Elastic Solid. J. Elas. 49, 31–63.

Rosen, B.W., 1967. Mechanics of Composite Strengthening. Fiber Compos. Mater. Soc. Met. Semin, 37–75.

Rudykh, S., Boyce, M.C., 2014. Transforming Wave Propagation in Layered Media via Instability-Induced Interfacial Wrinkling. Phys. Rev. Lett. 112, 34301.

Rudykh, S., deBotton, G., 2012. Instabilities of Hyperelastic Fiber Composites: Micromechanical Versus Numerical Analyses. J. Elast. 106, 123–147.

Shan, S., Kang, S.H., Raney, J.R., Wang, P., Fang, L., Candido, F., Lewis, J.A., Bertoldi, K., 2015. Multistable architected materials for trapping elastic strain energy. Adv. Mater. 27, 4296–4301.

Slesarenko, V., Rudykh, S., 2016. Harnessing viscoelasticity and instabilities for tuning wavy patterns in soft layered composites. Soft Matter 12, 3677–3682.

Su, T., Liu, J., Terwagne, D., Reis, P.M., Bertoldi, K., 2014. Buckling of an elastic rod embedded on an elastomeric matrix: planar vs. non-planar configurations. Soft Matter 10, 6294–6302.

Triantafyllidis, N., Maker, B.N., 1985. On the Comparison Between Microscopic and Macroscopic Instability Mechanisms in a Class of Fiber-Reinforced Composites. J. Appl. Mech. 52, 794.

Triantafyllidis, N., Nestorović, M.D., Schraad, M.W., 2006. Failure Surfaces for Finitely Strained Two-Phase Periodic Solids Under General In-Plane Loading. J. Appl. Mech. 73, 505.